

SN 2020jgb

AUTHORS¹

¹*Center for Interdisciplinary Exploration and Research in Astrophysics (CIERA), Department of Physics and Astronomy, Northwestern University, 1800 Sherman Road, Evanston, IL 60201, USA*

ABSTRACT

I am an abstract.

Keywords: We are the keywords

1. INTRODUCTION

It has been clear for decades that Type Ia Supernovae (SNe Ia) are caused by the thermonuclear explosions in carbon-oxygen (C/O) white dwarfs (WDs) in binary systems (see Maoz et al. 2014, for a review). Nevertheless, the nature of the binary companion, as well as how it ignites the WD, remains highly uncertain.

The helium-shell (He-shell) double detonation (DDet) scenario is one of the most promising channels to produce SNe Ia. In this scenario, the WD accretes from a companion to develop a helium-rich shell, which, once becomes massive enough, could detonate. Such a detonation sends a shock wave into the C/O core to trigger a runaway thermonuclear explosion and inevitably disrupt and destroy the entire WD (Nomoto 1982a,b; Woosley et al. 1986; Livne 1990; Woosley & Weaver 1994; Livne & Arnett 1995). The DDet mechanism can produce explosions in WDs below the Chandrasekhar mass (M_{Ch}).

There are several observational benchmarks for He-shell DDet triggered SNe. Shortly after the ignition of the shell, the decay of radioactive material in the helium ashes may power a detectable flash (Woosley & Weaver 1994; Fink et al. 2010; Kromer et al. 2010). The Fe-group elements in the ashes will blanket blue photons with wavelengths $\lesssim 5000 \text{ \AA}$ (Kromer et al. 2010), the duration of which depends on the mass of the He-shell. For thick enough shells, Boyle et al. (2017) suggest that the unburnt helium could provide an observational signal in near infrared (NIR) spectra, and Polin et al. (2021) predict significant [Ca II] emission in the nebular phase of the SNe.

Using different combos of He-shell mass and C/O core mass, one can reproduce a variety of observables in ‘normal’ SNe Ia with typical luminosities and spectral features near peak light (e.g., Polin et al. 2019; Shen et al. 2021), or peculiar sub-luminous ones (e.g., Polin et al. 2019).

For the DDet SNe that show ‘normal’ characteristics near their peaks, the mass of the He-shell is expected to be low ($\lesssim 0.03 M_{\odot}$; Kromer et al. 2010; Sim et al. 2010; Shen et al. 2018; Polin et al. 2019). The first DDet candidate with a thin He-shell is SN 2016jhr (Jiang et al. 2017), which exhibits an early red flash and keeps a red $g - r$ color throughout its evolution, though it show a typical absolute magnitude at peak ($M_g \approx -19$) for normal SNe Ia. The multi-band light curves involving the early flash and the major peak, as well as the optical spectrum close to the peak light, could be simultaneously fit by a near- M_{Ch} DDet model (a $1.38 M_{\odot}$ C/O core and a $0.03 M_{\odot}$ He-shell). Recently, a thinner He-shell is discovered in SN 2018aoz (Ni et al. 2022), a SN Ia showing a rapid redward color evolution within $\approx 12 \text{ hr}$ after the first light, which could be explained by a sub- M_{Ch} DDet model (a $1.05 M_{\odot}$ C/O core and a $0.03 M_{\odot}$ He-shell). After this red excess the photometry evolution is consistent with normal SNe Ia, when the ashes of the thin He-shell becomes optically thin. To date, only a small fraction of SNe Ia have been discovered early enough for possible detection of early flashes (e.g., Deckers et al. 2022). While there could be a large underlying population of normal SNe Ia triggered by He-shell DDet, it is hard to prove so.

In contrast, if the He-shell mass is much greater than $0.03 M_{\odot}$, the ashes of the He-shell detonation could remain optically thick in a much more extended phase, resulting in the red color and low luminosity near peak light. SN 2018byg (De et al. 2019) is a prototype of thick He-shell DDet SNe. During the late stages of preparing for this paper, Dong et al. (2022) presented another thick shell He-shell DDet candidates, SN 2016dsg, accompanied with an archival transient OGLE-2013-SN-079 (Inserra et al. 2015). All three candidates are faint, red, and show strong line-blanketing in maximum-light spectra. Dong et al. (2022) also report a tentative detec-

tion of unburnt helium in SN 2016dsg. The small sample size to date suggests thick shell events might be intrinsically rare.

It has been suggested that some, if not all, of the calcium-rich (Ca-rich) gap transients, a population of faint SNe with conspicuous [Ca II] emission in the nebular phase, also arise from He DDet [Chang: need to decide and consistently call these He-shell DDet, He DDet, or just DDet] (Dessart & Hillier 2015; De et al. 2020; Polin et al. 2021). A subclass of Ca-rich transients resemble SNe Ia near peak lights (termed Ca-Ia objects), marked by the strong Si II absorption and the absence of optical He I lines. There are only two Ca-Ia objects (SN 2016hmk and SN 2019ofm; De et al. 2020), both showing significant line-blanketing in spectra, and hence could be He-shell DDet objects. [Chang: Should cite Wynn’s paper somewhere in here] Nonetheless, they also exhibit properties of other types of sub-luminous SNe Ia, such as the strong O I absorption widely seen in 91bg-like objects (Filippenko et al. 1992) but not in other He-shell DDet candidates. Galbany et al. (2019) argue that SN 2016hmk is also consistent with a 91bg-like object arising from the deflagration of a near- M_{Ch} WD. In a word, the nature of Ca-Ia objects remain ambiguous. **Mention red Ca-Ib/c?**

In this paper, we present the observations of SN 2020jgb, another promising thick He-shell DDet candidate. This peculiar SN Ia highly resembles SN 2018byg in photometric and spectroscopic properties, and exhibits a remarkable feature in the NIR spectrum that could be attributed to the unburnt helium. In Section 2 we report the observations of SN 2020jgb, which are analyzed in Section 3, where we show its similarities with other He-shell DDet SNe and discuss the tentative He I absorption features. We use a grid of DDet models to fit the data of SN 2020jgb, and present the results in Section 4.1. In Section 4.3 we discuss the diversity in the host environments of DDet events. We draw our conclusions in Section 4. [Chang: the references are a little off here, but you can maybe get rid of those references anyway]

2. OBSERVATIONS

2.1. Discovery

SN 2020jgb was first discovered by the Zwicky Transient Facility (ZTF; Bellm et al. 2019; Graham et al. 2019) on 2020 May 03.463 UT (MJD 58972.463) with the 48-inch Samuel Oschin Telescope (P48) at Palomar Observatory. The automated ZTF discovery pipeline (Masci et al. 2019) detected SN 2020jgb using the image-differencing technique of Zackay et al. (2016). The candidate passed internal thresholds (e.g., Mahabal et al.

2019; Duev et al. 2019), leading to the production and dissemination of a real-time alert (Patterson et al. 2019) and the internal designation ZTF20aayhacx. It was detected with $g_{\text{ZTF}} = 19.86 \pm 0.15$ mag at $\alpha_{\text{J2000}} = 17^{\text{h}}53^{\text{m}}12^{\text{s}}.651$, $\delta_{\text{J2000}} = -00^{\circ}51'21''.81$ and announced to the public in Fremling (2020). The host galaxy, PSO J175312.663+005122.078, is a dwarf galaxy, to which SN 2020jgb has a projected offset of only $0.3''$. The last non-detection limits the brightness to $r_{\text{ZTF}} > 20.7$ mag on 2020 April 27.477 (MJD 58966.477; 5.99 days before the first detection). This transient was classified as a SNIa in Dahiwalé & Fremling (2020).

2.2. Host Galaxy Observations

We obtained a DEIMOS spectrum of the host galaxy, PSO J175312.663+005122.078, on 2022 March 31. The host exhibits strong, narrow emission lines including H α , H β , [N II] $\lambda 6583$, [O III] $\lambda 5007$, and [S II] $\lambda 6716$ & $\lambda 6731$. By fitting all these emission features with Gaussian profiles we obtain an average redshift of $z = 0.0309 \pm 0.0003$. With the diagnostic emission line equivalent width ratios ($\log [\text{N II}]/\text{H}\alpha = -1.19 \pm 0.07$ and $\log [\text{O III}]/\text{H}\beta = 0.53 \pm 0.06$), the host is consistent with star-forming galaxies in the BPT diagram (Baldwin et al. 1981; Veilleux & Osterbrock 1987).

To estimate the distance modulus to SN 2020jgb, we use the 2M++ model (Carrick et al. 2015) to obtain a peculiar velocity towards its host galaxy, PSO J175312.663+005122.078, to be 179 km s^{-1} . This, combined with the recession velocity in the frame of the cosmic microwave background¹ (CMB) $v_{\text{CMB}} = 9136 \text{ km s}^{-1}$, yields a net Hubble recession velocity of 9307 km s^{-1} , with a systematic uncertainty of 250 km s^{-1} [AAM: Dominated by the 2M++ cosmic flow?] [Chang: correct - you could even report pv as 179 ± 250]. Adopting $H_0 = 70 \text{ km s}^{-1} \text{ Mpc}^{-1}$, $\Omega_M = 0.3$, and $\Omega_\Lambda = 0.7$, we estimate the luminosity distance to SN 2020jgb to be 136.1 Mpc , which yields a distance modulus of $\mu = 35.66 \pm 0.06$.

2.3. Optical Photometry

SN 2020jgb was monitored in the g_{ZTF} and r_{ZTF} bands by ZTF as part of its ongoing Northern Sky Survey (Bellm et al. 2019). We adopt a Galactic extinction of $E(B - V) = 0.404$ mag (Schlafly & Finkbeiner 2011), and correct all photometry using the Fitzpatrick (1999) extinction model. We assume there is no additional extinction in the host galaxy. This assumption is supported by the lack of Na I D absorption at the redshift of the host galaxy, though see Poznanski et al.

¹ See https://ned.ipac.caltech.edu/velocity_calculator.

(2011) for caveats on the use of Na I D absorption as a proxy for extinction.

The forced photometry light curves² in absolute magnitudes in g_{ZTF} - and r_{ZTF} -bands are shown in Figure 1, in which we show all the measurements with $\text{SNR} > 2$. The light curves are reduced using the pipeline from Miller et al. (2022, in preparation). [Chang: Should also add a citation to Yuhan’s paper as a see also]

2.4. Optical Spectroscopy

We obtained optical spectroscopic follow-up of the object from ~ -10 days to $\sim +150$ days relative to the r_{ZTF} -band peak, using the Spectral Energy Distribution Machine (SEDm; Blagorodnova et al. 2018) on the automated 60 inch telescope (P60; Cenko et al. 2006) at Palomar Observatory, the Kast Double Spectrograph (Miller & Stone 1994) at the Shane 3 m Telescope, the Andaluia Faint Object Spectrograph and Camera (ALFOSC)³ installed at the Nordic Optical Telescope (NOT), the Double Beam Spectrograph (DBSP) on the 200 inch Hale telescope (P200; Oke & Gunn 1982), the Low Resolution Imaging Spectrograph (LRIS) on the Keck I telescope (Oke et al. 1995). Spectra were reduced using standard procedures (e.g., Matheson et al. 2000). Details of the spectroscopic observations are listed in Table 1, and the spectral sequence is shown in Figure 2.

On 2022 March 31, two years after the transient faded, we also took a spectrum for its host galaxy using the DEep Imaging Multi-Object Spectrograph (DEIMOS) on the Keck II telescope (Faber et al. 2003), for a total integration time of 3200 s. The spectra were reduced with the PyPeIt Python package (Prochaska et al. 2020).

2.5. Near-infrared (NIR) Spectroscopy

We obtained one NIR ($0.8\text{--}2.5\ \mu\text{m}$) spectrum of SN 2020jgb using the Gemini near-infrared spectrometer (GNIRS; Elias et al. 1998) on the Gemini North telescope on 2020 June 9 (~ 22 days after r_{ZTF} -band peak), for an integration time of 2400 s. The GNIRS spectrum was reduced with PyPeIt.

3. ANALYSIS

3.1. Photometric Properties

SN 2020jgb exhibited a fainter light curve than normal SNe Ia. In Figure 1, we compare the photometric properties of SN 2020jgb with the nearby, well-observed

Table 1. Spectroscopic Observations of SN 2020jgb and the host galaxy.

t_{obs}	Phase	Telescope/	R	Range	Air
(MJD)	(d)	Instrument	($\lambda/\Delta\lambda$)	(\AA)	Mass
58,976.42	−9.7	P60/SEDM	100	3770–9220	1.23
58,982.12	−4.2	NOT/ALFOSC	360	4000–9620	1.17
58,990.43	+3.9	P60/SEDM	100	3770–9220	1.23
58,997.44	+10.7	P60/SEDM	100	3770–9220	1.29
58,998.41	+11.6	Shane/Kast	750	3620–10720	1.28
59,008.41	+21.3	P60/SEDM	100	3770–9220	1.28
59,009.45	+22.4	Gemini-N/GNIRS	1800	8230–25150	1.07
59,010.40	+23.3	P200/DBSP	700	3200–9500	1.27
59,023.58	+36.1	Keck I/LRIS	1100	3200–10250	2.04
59,107.29	+117.3	Keck I/LRIS	1100	3200–10250	1.31
59,143.26	+152.2	Keck I/LRIS	1100	3200–10250	2.16
59,669.60	host	Keck II/DEIMOS	2100	4500–8700	1.14

NOTE—Phase is measured relative to the r_{ZTF} -band peak in the host galaxy rest frame. The resolution R is reported for the central region of the spectrum.

SN 2011fe (Nugent et al. 2011) and two He-shell DDet candidates, including the normal-luminosity thin shell candidate SN 2016jhr (Jiang et al. 2017) and the sub-luminous thick shell candidate SN 2018byg (De et al. 2019), with available photometric data on the Open Supernova Catalog⁴ (Guillochon et al. 2017). All these light curves have been corrected for Galactic reddening, while K -corrections have not been performed⁵. [Chang: I thought 11fe peaked brighter than −19.] [AAM: Double checked - essentially no Galactic extinction towards M101, so $M_g \approx 18.98$ mag. However, in the datafile from the open supernovae catalog, g-band light curves are referred to 2017MNRAS.472.3437G, where I couldn’t find the data.]

While the observational coverage is sparse in the rise to maximum light, from Figure 1 it is clear that SN 2020jgb is less luminous than normal SNe Ia (e.g., SN 2011fe). Furthermore, there is a flatter evolution in the r_{ZTF} evolution between -14 d and maximum light for both SN 2020jgb and SN 2020jgb than there is for SN 2011fe.

In the right panel of Figure 1, we compare the color evolution ($g-r$) of these objects relative to the measured time of first light t_{H} , accompanied by 62 normal SNe Ia (open circles) observed within 5 days of t_{H} by ZTF (from Bulla et al. 2020). For SN 2020jgb the early rise of the light curve was not well sampled, so we estimate t_{H} as

⁴ See <https://github.com/astrocatalogs/supernovae>.

⁵ These SNe were all observed in slightly different g - and r -bands.

² <https://web.ipac.caltech.edu/staff/fmasci/ztf/forcedphot.pdf>

³ <https://www.not.iac.es/instruments/alfosc/>

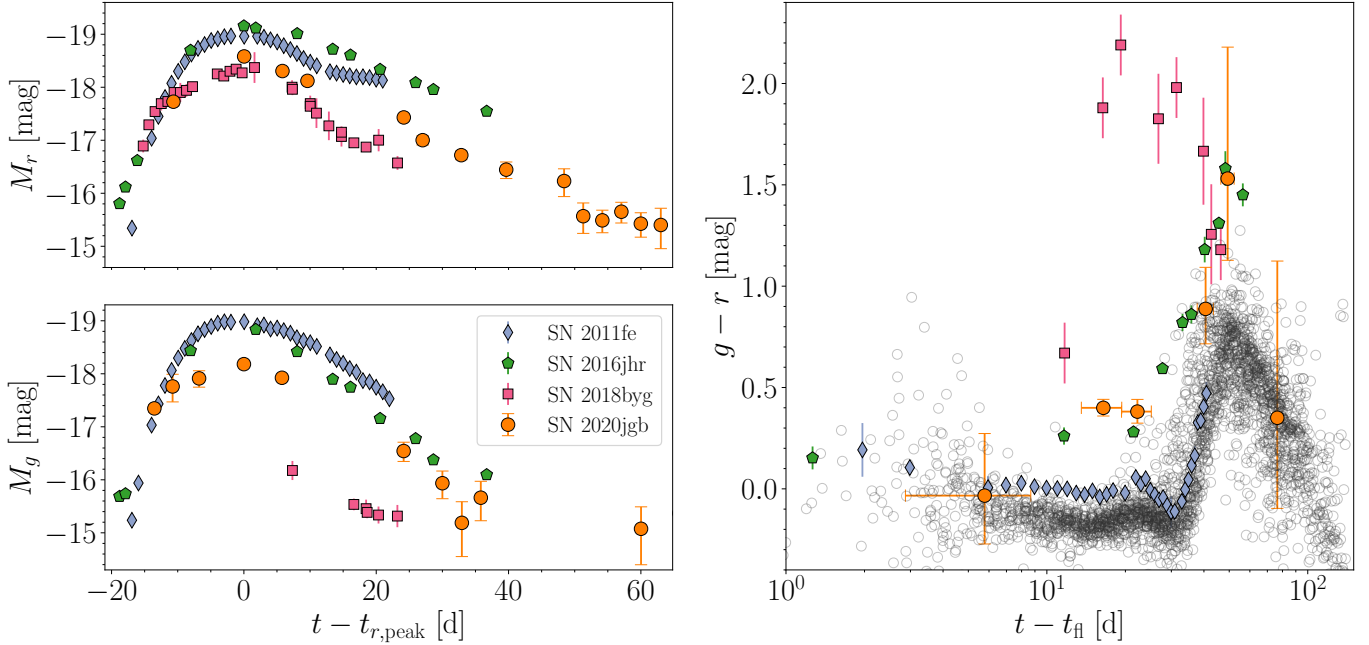


Figure 1. *Left:* Comparison of the multi-color light curves of SN 2020jgb with the normal SNe Ia SN 2011fe, the thin shell DDet candidate SN 2016jhr, and the thick shell DDet candidate SN 2018byg. The upper (lower) panel shows the evolution in g -band (r -band) absolute magnitudes. *Right:* comparison of $g - r$ color evolution to SN 2011fe and SN 2018byg, as well as 62 normal SNe Ia (open circles) with prompt observations within 5 days of first light by ZTF (Bulla et al. 2020).

the midpoint of the first detection and the last non-detection. We adopt an uncertainty on this estimate of 3 days. All three DDet candidates are undoubtedly redder than normal SNe Ia. At peak light, SN 2020jgb was not as red as the extreme case, SN 2018byg ($g - r \approx 2.2$ mag), but exhibited a similar color as SN 2016jhr ($g - r \approx 0.5$ mag).

3.2. Optical Spectral properties

In Figure 2, we show the optical spectral sequence of SN 2020jgb, and compare its spectra with some other SNe Ia near peak luminosity. For the spectra obtained after +100 d there is clear contamination from the host-galaxy, including the presence of narrow emission lines. For these spectra we subtract the galaxy light as measured in the DEIMOS spectrum from 2022 (see Section 2.4). The earliest spectrum was obtained by SEDM ≈ 10 days before the r_{ZTF} -band peak. We only show portions of the spectrum where the SNR > 2.5 , where the continuum is almost featureless with some marginal detection of the Si II $\lambda 6355$ at ≈ 6100 Å, the trademark of SNe Ia. In subsequent spectra the Si II features become more prominent and are clearly detected through +12 d. We measure Si II expansion velocities following a similar procedure as in Childress et al. (2013, 2014) and Maguire et al. (2014). The fitting region is selected by visual inspection. The continuum is assumed to be linear, and the absorption profile after the continuum nor-

malization is assumed to be composed of double Gaussian profiles peaked at 6347 Å and 6371 Å. Within the model, the continuum flux density at the blue and red edges are free parameters for which we adopt a normal distribution as a prior. The mean and standard deviation for the normal are the observed flux density and its uncertainty, respectively, at each edge of the fitting region. Three more parameters (amplitude, mean velocity, logarithmic velocity dispersion) are used to characterize the double Gaussian profile, whose priors are set to be flat. This means the depths and widths of both peaks are forced to be the same, as Maguire et al. (2014) has adopted in the optically thick regime. The priors of the three parameters are set to be flat. The Posteriors of the five parameters are sampled simultaneously with emcee (Foreman-Mackey et al. 2013) using the Markov chain Monte Carlo (MCMC) method. We find the mean expansion velocity is $\approx 11,500$ km s $^{-1}$ near maximum light.

In many SNe Ia the Ca II infrared triplet (IRT) absorption has two distinct components (Mazzali et al. 2005), which are conventionally referred to as photospheric-velocity features (PVFs) and high-velocity features (HVF). The PVFs originate from the main line-forming region with typical photospheric (i.e., bulk ejecta) velocities, while the HVFs are blueshifted to much shorter wavelengths, indicating significantly higher (by greater than ~ 6000 km s $^{-1}$) velocities than typical PVFs (Silverman et al. 2015). Figure 2 shows

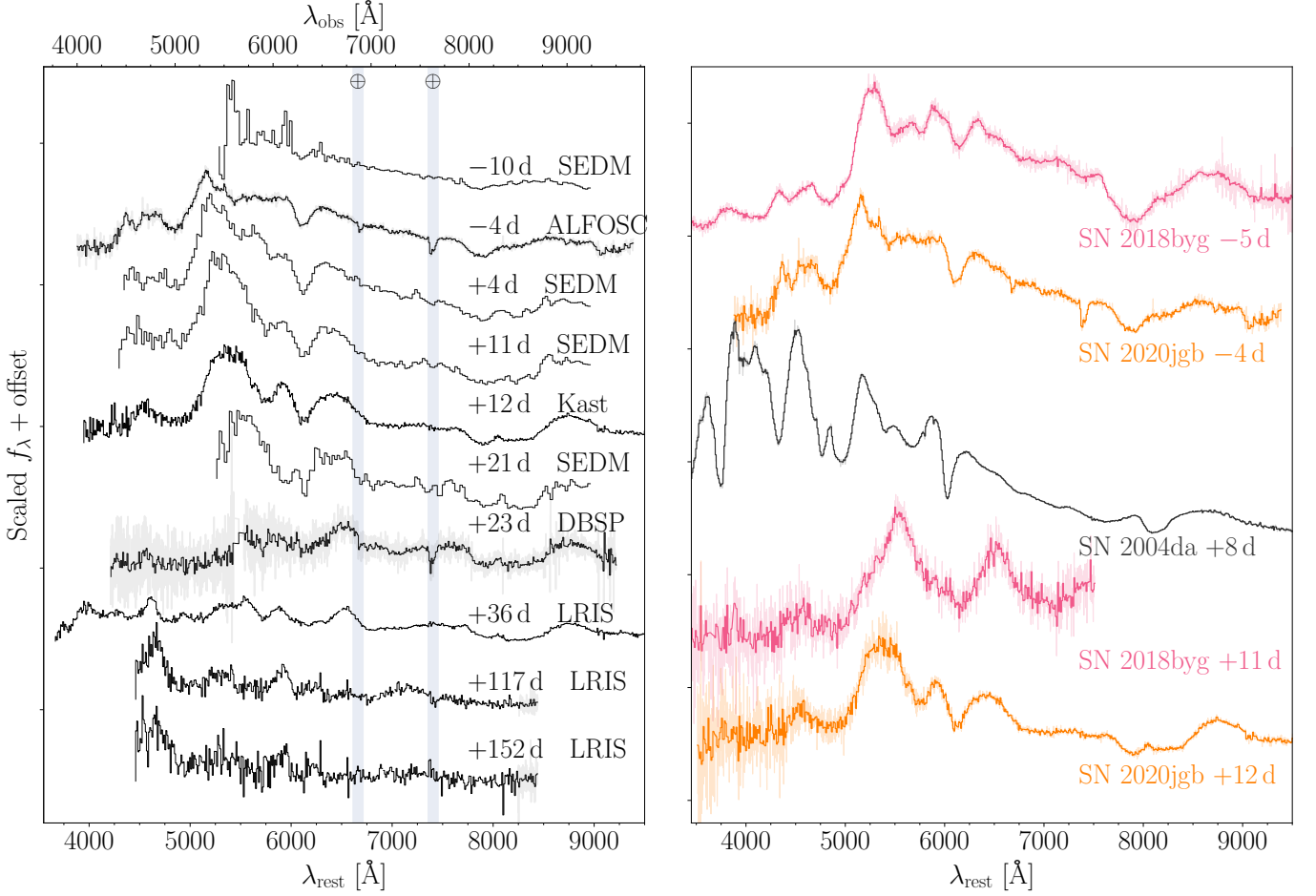


Figure 2. *Left:* optical spectral sequence of SN 2020jgb. Rest frame phases (days) relative to the r_{ZTF} -band peak and instruments used are posted next to each spectrum. The spectra are after Galactic extinction correction are shown in grey. The black lines are binned spectra with a bin size of 10 \AA , except for the SEDM spectra, whose resolution is lower than the bin size. In the last two spectra, we have subtracted the light from the host galaxy. Only regions with $\text{SNR} > 2.5$ after binning are plotted. *Right:* spectral comparison with SN 2018byg (sub-luminous He-shell DDet; De et al. 2019) and SN 2004da (normal luminosity; Silverman et al. 2012).

that SN 2020jgb has prominent HVFs of Ca II IRT. The HVFs are visible in our first spectrum of SN 2020jgb, and remain prominent through +36 days. Using a similar technique in modeling the Si II features, we fit the HVFs and PVFs simultaneously. Both are fit by multiple Gaussian profiles assuming each line in the triplet can be approximated by the same profile (i.e., same amplitude and velocity dispersion). A best-fit expansion velocity of HVFs is $\gtrsim 26,000 \text{ km s}^{-1}$. A clear delineation between the HVFs and PVFs is visible ≈ 4 days before peak light. Since then we fit the broad absorption features with two different velocity components simultaneously. The velocity of HVFs slightly declines but stays above $\approx 24,000 \text{ km s}^{-1}$, and the velocity of PVFs declines from $\approx 11,000 \text{ km s}^{-1}$ to $\approx 9,000 \text{ km s}^{-1}$. As in normal SNe Ia, the relative strength between the HVFs and PVFs decreases with time. [Chang: might be worth

a figure - especially if we have this measured for several other DDet now]

The nebular phase spectra of SN 2020jgb are dominated by the Fe-group elements, showing some enhancement in flux between ≈ 4500 and $\approx 6000 \text{ \AA}$. We did not detect any emission feature related to [Ca II] $\lambda\lambda 7291, 7324$, which is a hallmark for Calcium-rich gap transients and is also prominent in a few DDet candidates (e.g., SN 2016hmk and SN 2019ofm; De et al. 2020).

The optical spectral evolution of SN 2020jgb resembles that of SN 2018byg, a sub-luminous DDet with a thick He-shell. At early times, both SNe were relatively blue and featureless with broad and shallow Ca II IRT absorption. As they evolved closer to maximum light, they developed strong continuous absorption bluewards of $\approx 5000 \text{ \AA}$, while the Si II $\lambda 6355$ and the Ca II IRT became more prominent. S II was not detected in either

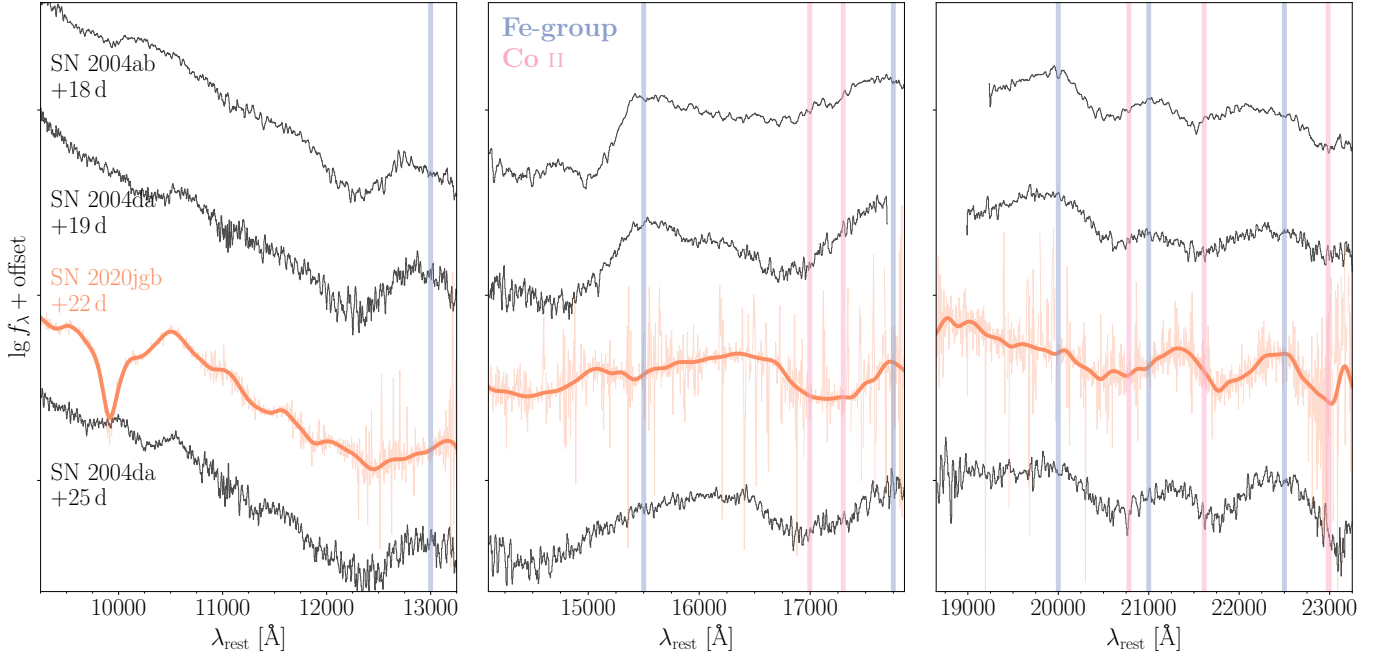


Figure 3. The NIR spectra of SN 2020jgb and two SNe Ia with normal maximum luminosity (SN 2004ab and SN 2004da, Marion et al. 2009), taken about three weeks after the peak. For each spectrum, the continuum at $\gtrsim 1.2 \mu\text{m}$ is significantly reshaped by the Fe-group blanketing (emission features, blue vertical lines) and Co II absorption (pink vertical lines). Spectra for SN 2004ab and SN 2004da are obtained from Marion et al. (2009). [Chang: what velocity is assumed for Fe and Co? Some of the lines do not “line up”?]

object. In the DDet scenario, a large amount of Fe-group elements will be synthesized in the outer regions of the ejecta, which will cause significant line-blanketing near maximum light (Kromer et al. 2010; Polin et al. 2019), and also high velocity intermediate-mass elements like Ca II (Fink et al. 2010; Kromer et al. 2010). The similarity between SN 2020jgb and SN 2018byg, makes SN 2020jgb another promising DDet SN candidate.

SN 2004da is a normal SN Ia that shows similarities to SN 2020jgb in the NIR (Section 3.3), however, the two SNe are extremely different in the optical (Figure 2). From this comparison it is clear that SN 2020jgb is not a normal SN Ia.

3.3. NIR Spectral properties

The NIR spectrum of SN 2020jgb is compared with two normal SNe Ia at a similar phase in Figure 3 (data for SNe 2004ab and 2004da from Marion et al. 2009). SN 2020jgb shows a strong absorption feature at $\sim 0.99 \mu\text{m}$, which is not seen in normal SNe Ia. This feature was still significant two weeks later, as detected by LRIS on Keck (see Figure 6), though it was only partially covered. Aside from this prominent feature, SN 2020jgb resembles normal SNe Ia in NIR band. The shape of the continuum redwards to $\approx 1.2 \mu\text{m}$ is significantly altered by line-blanketing from Fe-group elements. Just like normal SNe Ia, SN 2020jgb shows an

enhancement of flux at about 1.3, 1.55, 2.0, 2.1, and $2.25 \mu\text{m}$, accompanied by several Co II absorption lines. It is especially similar to SN 2004da at +25 days after maximum light as the steep increase in flux at $\approx 1.55 \mu\text{m}$, known as the *H*-band break (Hsiao et al. 2019), has become less prominent.

In a sample of 15 spectra for normal SNe Ia between +14 days and +75 days after the peak light, not a single one shows such a prominent absorption features around $1 \mu\text{m}$ Marion et al. (2009). We have investigated several potential identifications for this feature (see below), however, none of them provide a fully satisfying explanation.

The most tantalizing possibility is that the absorption is due to He I $\lambda 10830$. If SN 2020jgb is a DDet SN, then unburned He could lead to observed absorption in the spectrum, as shown in the sub-Chandrasekhar-mass He-shell DDet models of Boyle et al. (2017). Figure 6 shows that the $1 \mu\text{m}$ feature, if associated with He I $\lambda 10830$, has a high velocity ($\approx 26,000 \text{ km s}^{-1}$), especially considering the phase of the SN. The Ca II IRT also exhibits similarly high velocities at the same phase ($\approx 24,000 \text{ km s}^{-1}$), suggesting it is not impossible to see very high absorption velocities at this phase. The expansion velocity in the ejecta is roughly linearly proportional to the radius, so such a high velocity indicates that both the Ca II IRT and the tentative He I absorp-

tion line form far outside the normal photosphere, which has a velocity of only $\approx 10,000 \text{ km s}^{-1}$. In this sense, the He-shell DDet scenario, in which the unburnt helium is located in the outermost ejecta, is indeed supported.

We cannot claim an unambiguous detection of He I, however, as our spectra lack definitive absorption from other He I features that we would expect to be prominent, such as He I $\lambda 20581$. Considering a line velocity of $\approx 26,000 \text{ km s}^{-1}$ and a host galaxy redshift of 0.0309, this line will be blueshifted to $\approx 1.95 \mu\text{m}$ in the observer frame, so will be strongly blended by the strong telluric lines within $1.8\text{--}2.0 \mu\text{m}$. After telluric correction, the signal to noise ratio reaches ~ 5 , with which we still cannot see any significant absorption feature. An upper limit of the equivalent width is determined to be $< 2\%$ of the He I $\lambda 10830$ line, while theoretically, the 20581 line is supposed to be only a factor of 6–12 weaker, depending on temperature (Marion et al. 2009). Another fact is that the $1 \mu\text{m}$ feature is as strong as the He I $\lambda 10830$ in many helium-rich core-collapse supernovae, say, Type Ib supernovae, in which the He I $\lambda 20581$ line is weaker than the He I $\lambda 10830$ line yet still prominent (Shahbandeh et al. 2022). In one of the models in Boyle et al. (2017), there is no obvious He I $\lambda 20581$ absorption in the synthetic spectra (see their Figure 7), but the model is intended to be representative for normal-luminosity SNe Ia. If the $1 \mu\text{m}$ feature is associated with He I, it would be very unusual if the $2 \mu\text{m}$ feature is not seen at all, even if somehow blended by the telluric lines.

Other possible identifications include Mg II $\lambda 10927$, C I $\lambda 10693$, and Fe II $\lambda 10500$ & $\lambda 10863$. The Mg II $\lambda 1.0927 \mu\text{m}$ line is prevalent in the NIR spectra of SNe Ia, but usually disappears within a week after peak (Marion et al. 2009), while the $1 \mu\text{m}$ feature was still visible over a month after the peak in the Keck LRIS spectrum. The required radial velocity is $\approx 30,000 \text{ km s}^{-1}$, $\approx 20\%$ faster than the HVFs of Ca II IRT at the same phase. While such a high velocity for Mg II has never been seen in other SNe Ia, since high-velocity intermediate-mass elements like magnesium and calcium can be synthesized by the detonation of helium shell (Shen & Moore 2014), the Mg II origin of the $1 \mu\text{m}$ feature cannot be strictly ruled out. But if we attribute this $1 \mu\text{m}$ feature to high-velocity Mg II, we would expect an even stronger Mg II $\lambda 9227$ line to be blueshifted to the red edge of the Ca II IRT, which is not detected. Given the strength of the $1 \mu\text{m}$ feature, the Mg II $\lambda 9227$ line should not be completely obscured by the Ca II IRT features.

C I $\lambda 10693$ is not observed as frequently as Mg II $\lambda 10927$ in SNe Ia. Hsiao et al. (2019) presented a sample of five SNe Ia with C I detections, showing the C I fea-

ture is strongest for fainter, fast-declining objects. However, in their sample, the C I feature is a pre-maximum feature which fades away as the luminosity peaks, so the discrepancy in phase is large. The required expansion velocity $\approx 22,000 \text{ km s}^{-1}$, which is overwhelmingly faster than the estimated carbon velocity for the sample in Hsiao et al. (2019) ($\sim 10,000\text{--}12,000 \text{ km s}^{-1}$), but still consistent with the HVFs of Ca II IRT. Nonetheless, no significant carbon absorption is detected in the optical band.

The Fe II features in SNe Ia usually start to develop roughly three weeks after the peak, which is about the same phase as we obtained our GNIRS spectrum. Two Fe II lines, $\lambda 9998$ and $\lambda 10500$, are actually visible on the blue/red wings of the $1 \mu\text{m}$ feature. The Fe II $\lambda 10863$ line is not yet seen in the GNIRS spectrum. They correspond to an expansion velocity of $\approx 8,000 \text{ km s}^{-1}$, which is consistent with the PVFs of the Ca II IRT at the same epoch. They also match the same two lines for normal SNe Ia (Marion et al. 2009), making the identification more reliable. Obviously, these two Fe II features are wider and shallower than the strong feature between them. We fit the $1 \mu\text{m}$ feature with three Gaussian profiles. Two of them are set to be the blueshifted Fe II $\lambda 9998$ and $\lambda 10500$, and the other is an uncorrelated Gaussian profile which mainly describes the absorption in the center. We find that the shallower and wider Fe II lines only make up $\sim 40\%$ of the total equivalent width, and the rest $\sim 60\%$ comes from the central feature, which cannot be accounted for by any Fe II feature at the same velocity. Given the similarity of the Fe-group line-blanketing between the GNIRS spectrum with the spectrum of SN 2004da at +25 days, the distribution of Fe-group elements inside each supernova ejecta should be somehow similar as normal SNe Ia, so the central region of the $1 \mu\text{m}$ feature is not likely to be associated with Fe II either.

4. DISCUSSION

4.1. Models

A few sentences from Abi describing the models.

In Figure 4, we show the comparison of the photometric and spectroscopic features of SN 2020jgb with DDet models from Polin et al. (2019). The peak luminosity reflects the total progenitor mass (C/O core + He shell), and we find models with a total mass of $0.95 M_{\odot}$ generally reproduce the r -band peak brightness well. Thus in Figure 4, the total mass is fixed to be $0.95 M_{\odot}$ in all models. The overall r -band photometric evolution is best fit by the model with a $0.87 M_{\odot}$ C/O core and a $0.08 M_{\odot}$ He shell, while all three models underestimate the g -band brightness after the peak. This deviation

may be attributed to a variety of factors on handling the explosion and radiative transfer. First, throughout the simulations we assume local thermodynamic equilibrium (LTE), which is not valid once the ejecta becomes optically thin. Typically the bulk ejecta of a sub- M_{Ch} SNe Ia remains optically thick for ~ 30 days since the explosion. But in modeling the brightness in g -band, the LTE assumption is even more tricky, because the major opacity in g -band comes from the Fe-group line-blanketing in the outermost ejecta, where the optical depth may evolve differently from that at the photosphere. Hence the LTE condition may quickly become inapplicable. Furthermore, our 1-D He shell model is not capable to capture the multi-dimensional effects in the explosion such as asymmetries. The viewing angle is known to have a significant influence on the observed light curves (Kromer et al. 2010; Sim et al. 2012; Gronow et al. 2020; Shen et al. 2021), especially in bluer bands where the line-blanketing depends sensitively on the distribution of He-shell ashes (Shen et al. 2021). In previous studies on other DDet objects, the g -band brightness is systematically under-predicted shortly after the peak, despite the fact that redder bands can be fit decently (e.g. Jiang et al. 2017; Jacobson-Galán et al. 2020) [Chang: typo in Wynn's name].

The model which best fits the photometry ($0.87 M_{\odot} + 0.08 M_{\odot}$) also reproduces the major absorption features (e.g., Fe-group line-blanketing, Si II $\lambda 6355$, PVFs of Ca II IRT) and the corresponding expansion velocities near the peak light. However, we are not able to fit the continua in g -, r -, and z -bands simultaneously, and the strong Ca II HVFs are not seen in the synthetic spectrum. These discrepancies could also be due to the asymmetry in the DDet, that SN 2020jgb was observed fairly close to the ignition point, where the abundances of Fe-group elements and high velocity calcium synthesized in the shell could be much higher than an angle-averaged 1-D model would predict. In addition, the predicted Si II $\lambda 5972$ does not show up in the observed spectrum.

Conclusions from the model comparison.

4.2. The $1 \mu\text{m}$ Feature

While the nature of the $1 \mu\text{m}$ feature remains uncertain, other He-shell DDet candidates also seem to show similar complexity in this region. In the currently small sample of six candidates, three objects (SN 2016jhr, SN 2018aoz, and SN 2019ofm) do not have any available NIR spectra, while the other three (at quite different phases though) all exhibit strong absorption features near $1 \mu\text{m}$, as shown in Figure 5. SN 2016hmk has two deep absorption features around $1.02 \mu\text{m}$ and $1.17 \mu\text{m}$,

both are at a longer wavelength than the $1 \mu\text{m}$ feature in SN 2020jgb. Galbany et al. (2019) suggest both of them could be caused by Fe II, though they are deeper than in other SNe Ia. The velocity of the $1.02 \mu\text{m}$ feature is $\approx 21,000 \text{ km s}^{-1}$ assuming a He I $\lambda 10830$ origin, which, just like SN 2020jgb, is about the same as the HVFs of the Ca II IRT in the optical spectra (see Figure 6). The PVFs of the Ca II IRT of both SNe have a similar expansion velocity of $\approx 10,000 \text{ km s}^{-1}$. Such a consistency in velocities is also seen in SN 2018byg (see Figure 6). The large width and lower signal-to-noise ratio for the $1 \mu\text{m}$ feature in SN 2018byg makes it difficult to determine an exact line velocity. This feature is likely to be a mixture of several different lines.

Dong et al. (2022) recently presented another thick He-shell DDet candidate, SN 2016dsg, with an absorption line around $\sim 0.97\text{--}1.05 \mu\text{m}$ in a low-SNR NIR spectrum at +16.6 days.⁶ Assuming He I $\lambda 10830$ origin, the minimum of the absorption profile (at $\approx 1.03 \mu\text{m}$, see Figure 4 in Dong et al. 2022) corresponds to an expansion velocity of $\approx 15,000 \text{ km s}^{-1}$, lower than the $1 \mu\text{m}$ features in SN 2020jgb, SN 2016hmk, and SN 2018byg assuming their He I origin. Interestingly, SN 2016dsg shows the least prominent HVFs of Ca II IRT among the four, which also has a low velocity of $\approx 15,000 \text{ km s}^{-1}$. Once again, the scenario where both the unburnt helium and the high velocity calcium are located at the outermost shell is favored.

Unfortunately, none of the spectra for SN 2016dsg, SN 2016hmk, or SN 2018byg covers the $2 \mu\text{m}$ region, thus it is not possible to identify the presence of helium decisively. But if the $1 \mu\text{m}$ feature of these objects are of the same origin, they are more likely to be correlated with the high velocity ejecta lying in the outmost region in the supernovae, because at least for SN 2020jgb and SN 2016hmk, the difference in their photospheric velocities cannot explain the discrepancy in their line velocities of the $1 \mu\text{m}$ feature. Then helium is still a promising candidate to cause strong absorption near $1 \mu\text{m}$ for these sub-luminous He-shell DDet SNe Ia.

In conclusion, from all the He-shell DDet candidates with NIR spectra available, we have detected strong absorption features near $1 \mu\text{m}$, which is not seen in normal SNe Ia. Indeed, these candidates have their NIR spectra taken at different epochs, hence each $1 \mu\text{m}$ feature can be of completely unrelated origin. Had they all originate from He I $\lambda 10830$, there would still be large diversity in the corresponding expansion velocities. This is to be

⁶ SN 2016dsg was discovered on the decline. The phase is relative to the discovery time.

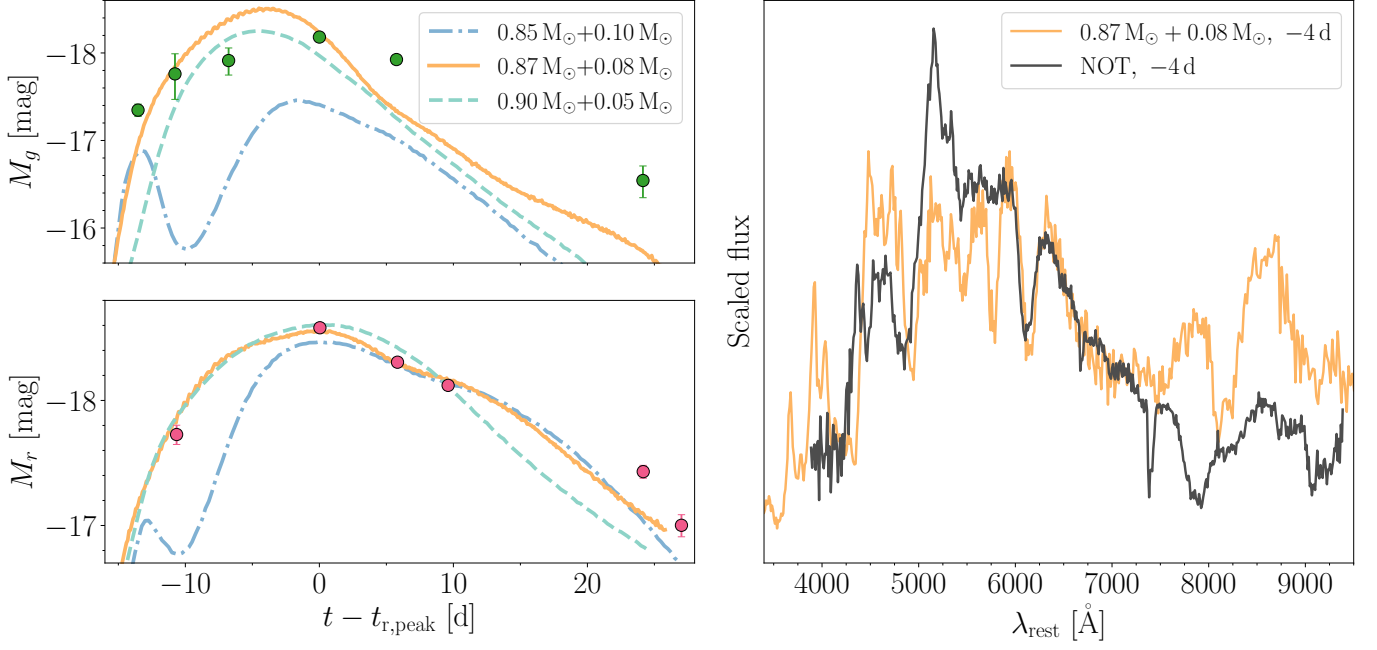


Figure 4. *Left:* Comparison of the photometric evolution of SN 2020jgb with the He-shell DDet models from Polin et al. (2019). The model parameters are indicated in the legend as (C/O core mass + He shell mass). The upper (lower) panel shows the evolution in g -band (r -band) absolute magnitudes. *Right:* Comparison of the spectrum of SN 2020jgb with the $0.87 M_{\odot}$ C/O core + $0.08 M_{\odot}$ He-shell DDet model before peak luminosity. Each spectrum is normalized by the median flux between 6500 and 7500 Å, and binned with a size of 10 Å. The synthetic spectrum 4 days before the r -band peak best matches the NOT spectrum (Galactic extinction corrected), which was obtained ~ 4 days before the r_{ZTF} -band peak. All the phases have been rescaled to the host galaxy rest frame.

confirmed in a more complete NIR spectral sequence in future He-shell DDet SNe Ia. Nonetheless, the apparently ubiquitous $1 \mu\text{m}$ features in various phases is possibly a distinctive attribute against normal SNe Ia.

4.3. Host Environments

We model the stellar population of the host galaxy of SN 2020jgb using *prospector* (Johnson et al. 2021), a package for principled inference of stellar population properties using photometric and/or spectroscopic data. The input data included the Galactic extinction corrected DEIMOS spectrum, as well as the archival photometric data from the Panoramic Survey Telescope and Rapid Response System (Pan-STARRS; Chambers et al. 2016, r , i , z Kron magnitudes) and the VISTA Hemisphere Survey (VHS; McMahon et al. 2013, J and K_s Petrosian magnitudes). In the best fit, the estimated stellar mass is $\log(M_* [M_{\odot}]) = 7.79^{+0.07}_{-0.06}$, and the specific star-formation rate (sSFR) is $\log(\text{sSFR} [\text{yr}^{-1}]) = -10.25^{+0.09}_{-0.08}$, with the uncertainties denoting the 68% credible regions.

In Figure 7, we show the sSFR and the stellar mass for the host galaxies of six He-shell DDet candidates. Again using *prospector*, we fit the stellar properties for all the other candidates with optical spectra from the Sloan Digital Sky Survey (SDSS; York et al. 2000)

and photometry from the DESI Legacy Imaging Surveys (Dey et al. 2019, g , r , z , W_1 , W_2 , W_3 , W_4 magnitudes). With mid-infrared photometry available, *prospector* can better estimate the overall dust extinction in the host galaxy and the contribution of an active galactic nucleus (AGN) to the spectral energy distribution (SED). Unfortunately, two (SN 2016hmk and SN 2019ofm) out of six hosts are close-by ($z \lesssim 0.03$) late-type galaxies with extended, spatially resolvable spiral structures. In both surveys, only photons from their red, concentrated bulges were fed to the detectors, while the lights from the blue, diffuse star-forming regions were completely missed. We would inevitably underestimate their SFR should we naively fit the SEDs from these surveys. Therefore, for the host of SN 2016hmk, we adopt the results in Galbany et al. (2019) as part of the PMAS/PPak Integral-field Supernova Hosts Compilation (PISCO; Galbany et al. 2018), where the photons from the H II regions in the spiral arms were also collected using integral field spectroscopy (IFS). For the host of SN 2019ofm, there are no IFS data available, so we still show our best-fit stellar mass and sSFR in Figure 7, with the caveat that the sSFR should be regarded as a lower limit. The host of SN 2018aoz (NGC 3923) is a local ($z = 0.00580$) early-type galaxy and is outside

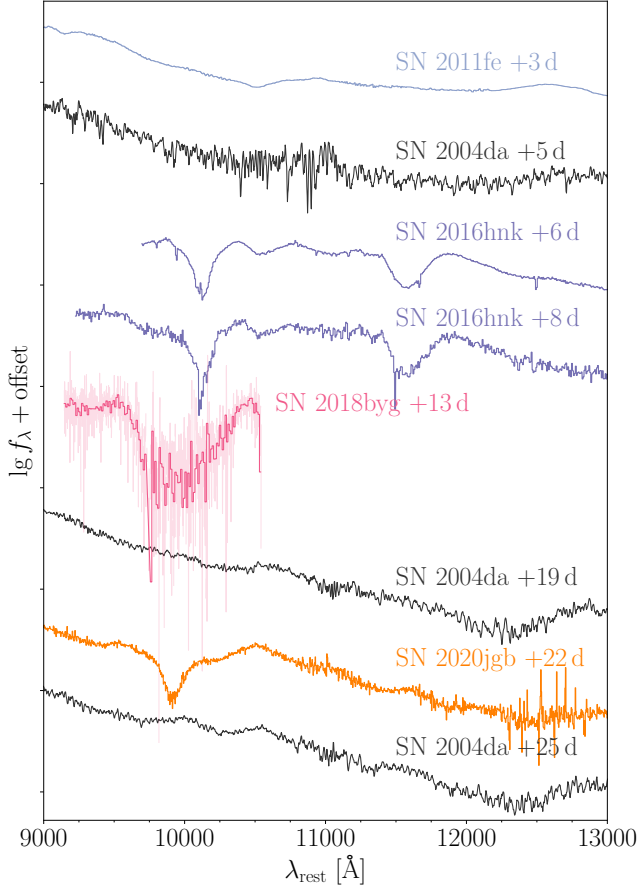


Figure 5. The NIR spectra (9000 to 13000 Å) of a few normal SNe Ia (SN 2011fe and SN 2004da) and three He-shell DDet candidates, which are all sub-luminous SNe Ia (SN 2016hmk, SN 2018byg, and this source, SN 2020jgb). Other than the spectrum of SN 2004da, all spectroscopic data are obtained from the WISEReP repository (Yaron & Gal-Yam 2012).

the SDSS footprint, so we adopt its stellar population properties from the Census of the Local Universe (CLU) catalog [AAM: References?].

With only a handful of He-shell DDet objects classified, they have been discovered in all kinds of host environments. Figure 7 reveals that DDet SNe emerge in both star-forming and passive galaxies, which is true for both thin He-shell objects of normal luminosity (SN 2016jhr in a star-forming host; SN 2018aoz in a passive host) and thick He-shell, sub-luminous objects (SN 2020jgb in a star-forming host; SN 2018byg in a passive host), even when the natures of SN 2016hmk and SN 2019ofm remain ambiguous. There are also diversities in their locations in their hosts. SN 2020jgb has a small projected physical offset (~ 0.2 kpc) to the center of its host, a star-forming dwarf galaxy, so it is highly likely to originate from a young, star-forming environ-

ment. SN 2016hmk has a moderate projected host offset (~ 4 kpc) and a potential origin in an H II region with ongoing star-formation (Galbany et al. 2019). SN 2019ofm has a large projected offset (~ 11 kpc) but is still on the blue, diffuse spiral arm [AAM: How can I refer to the DECaLS image?]. Other objects, including the recently discovered SN 2016dsg and OGLE-2013-SN-079 (Dong et al. 2022), show large projected host offsets ($\gtrsim 10$ kpc) and lie in the galaxy outskirts, which usually indicates origin in old stellar population.

In this sense, the He-shell DDet sample resembles the normal SNe Ia population, which can occur in both star-forming and quenched galaxies (e.g., Sullivan et al. 2006; Smith et al. 2012), and is very different from some other types thermonuclear supernovae, such as Type-Iax supernovae (SNe Iax) which almost only appear in star-forming galaxies, or SN 1991bg-like and SN 2002es-like objects, which prefer old stellar environments (see the review in Jha et al. 2019). This favors the postulated sequence that He-shell DDet SNe may make up a substantial fraction of the normal SNe Ia, which is supported by studies on stellar metallicity observations (Eitner et al. 2022) or stellar population synthesis (need references).

The diversities in host environments indicate multiple formation channels in the He-shell DDet SNe population. Those in the star-forming environments, SN 2020jgb being the most unambiguous example, could originate from some analogues of the two subdwarf B binaries with WD companions (Geier et al. 2013; Kupfer et al. 2022) discovered in young stellar populations. On the other hand, those with large host offsets could not be easily formed *in situ*. Similarly, many Ca-rich transients are also observed in remote locations (Lunnan et al. 2017), for which some dynamical formation channels have been proposed. To reach the outskirts of galaxies, WD binaries would need to be hardened and ejected by globular clusters (Shen et al. 2019) or supermassive black holes (Foley 2015) before explosions. Given that some Ca-rich transients show characteristic DDet properties (De et al. 2020), these channels may also be applicable to some of the He-shell DDet SNe.

The robust detection of SN 2020jgb in a star-forming region also agrees with independent studies on SNe Ia progenitors using stellar metallicity observations. de los Reyes et al. (2020), by studying the manganese abundances in dwarf spheroidal satellites of the Milky Way, argue that sub- M_{Ch} SNe Ia dominates the chemical evolution of a galaxy, while near- M_{Ch} SNe tend to take over at later times. This indicates that observationally, sub- M_{Ch} SNe Ia might have a stronger preference towards younger stellar populations than near- M_{Ch} SNe

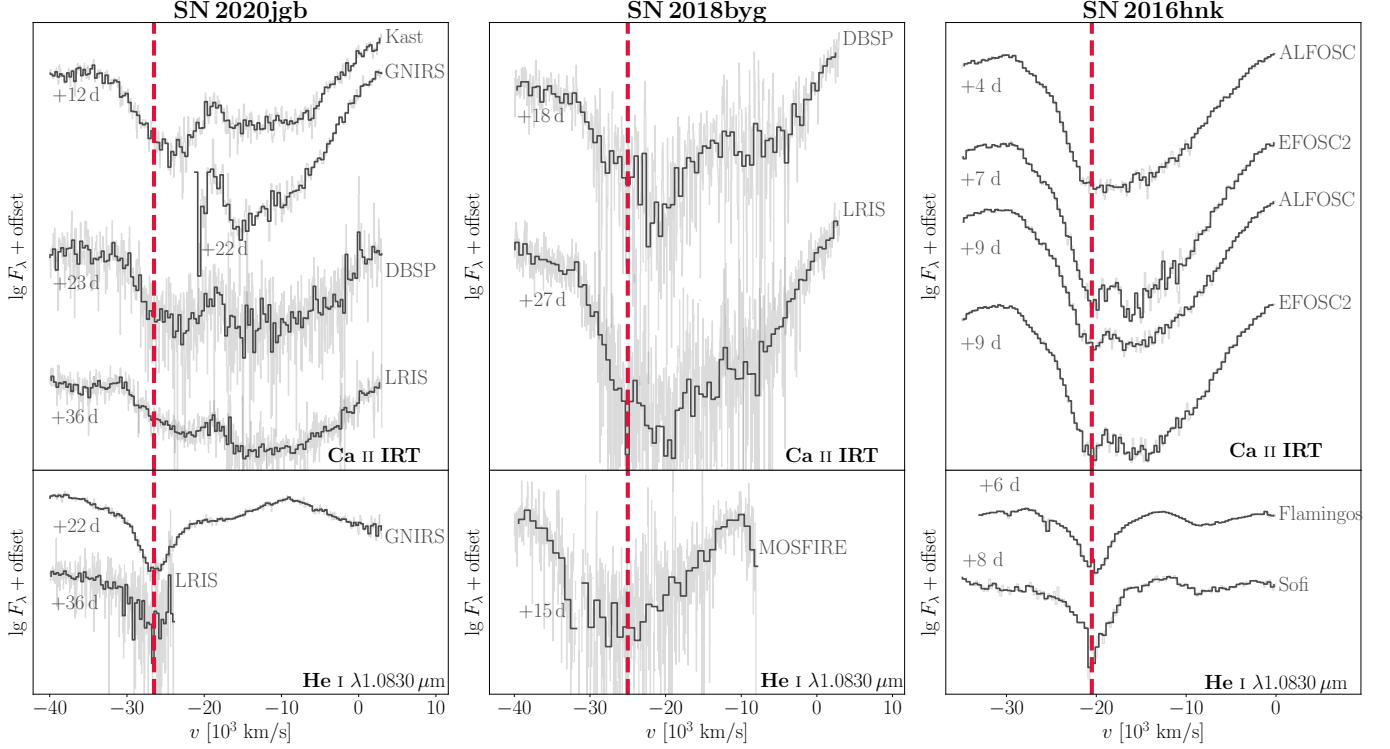


Figure 6. Spectra of SN 2020jgb, SN 2018byg, and SN 2016hbk in the velocity space, comparing the Ca II IRT absorption features (upper panels) and the $1\mu\text{m}$ features assuming they are associated with He I $\lambda 10830$ (lower panels). The red dashed lines mark the minimum of each $1\mu\text{m}$ feature. Data for SN 2018byg and SN 2016hbk are obtained from the WISEReP repository (Yaron & Gal-Yam 2012). [Chang: add statement about “guide the eye”]

Ia. Since He-shell DDet is one of the most favored channel to ignite a sub- M_{Ch} WD, we would expect the majority of exploded SNe Ia in star-forming galaxies (at least the dwarfs) would undergo DDet. We note that while SN 2020jgb is the first confirmed He-shell DDet SN in a star-forming dwarf, which indicates that thick shell DDet SNe might be intrinsically rare, the same may not be true for thin shell DDet SNe since they would look just as *normal* a few days after explosions (Ni et al. 2022). Unfortunately, few of them are observed in such an early phase to date (SN 2016jhr and SN 2018aoz being two of them), thus we might have missed a great number of He-shell DDet SNe. With more efficient time domain surveys kicking in in the near future and prompt follow-up observations being increasingly available, a systematic studies on the infant SNe Ia will help confirm this implication.

5. CONCLUSIONS

In the paper, we have presented the observations of SN 2020jgb, a peculiar SN Ia. Putting together its low luminosity, red $g-r$ color, and strong line-blanketing in the spectra near peak light, we show it bears a high degree of resemblance to SN 2018byg (De et al. 2019), whose observational properties could be explained by

the detonation of a shell of helium on a sub- M_{Ch} WD. Fitting the light curves of SN 2020jgb to a grid of models in Polin et al. (2019), we show a $\approx 0.87 M_{\odot}$ WD beneath a $\approx 0.08 M_{\odot}$ He-shell would be a reasonable estimate on its progenitor properties.

A high-SNR NIR spectrum obtained three weeks after the peak light shows a prominent absorption feature near $1\mu\text{m}$, which could be produced by the unburnt helium (He I $\lambda 10830$) in the outermost ejecta expanding at a high velocity ($\approx 26,000 \text{ km s}^{-1}$). At the same epoch, the Ca II IRT also exhibits similarly high velocities ($\approx 24,000 \text{ km s}^{-1}$). By now, we have a very small sample of four candidate He-shell DDet SNe which have NIR spectra observed. Interestingly, all of them show deep absorption features near $1\mu\text{m}$, which, if assumed to have a helium origin, would be expanding very a similar HVFs velocity of Ca II IRT, despite the huge diversity in velocities (from $\approx 15,000 \text{ km s}^{-1}$ in SN 2016dsg to $\approx 24,000 \text{ km s}^{-1}$ in SN 2020jgb). If it is the unburnt helium and the newly synthesized calcium from the He-shell that produce these line features, such a consistency in the expansion rates of different absorption lines would be naturally explained. However, we could not find unambiguous evidence for other He I absorption, such as He I $\lambda 20581$, so we are not drawing a definitive conclu-

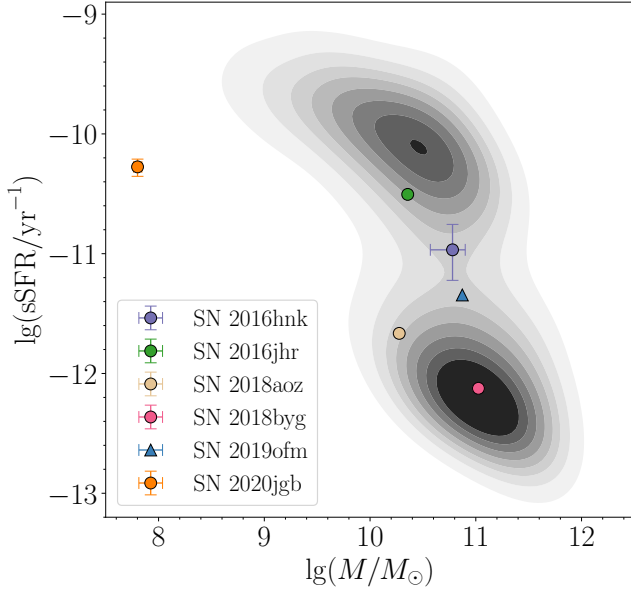


Figure 7. The specific star-formation rate (sSFR) and the stellar mass for the host galaxies of He-shell DDet candidates. The properties for the hosts of SN 2016hmk and SN 2018aoz are taken from Galbany et al. (2019) and the CLU catalog [AAM: References?], respectively. For the sSFR in the host of SN 2019ofm, only a lower limit is shown (the triangle). The background is a sample of galaxies from the SDSS MPA-JHU DR8 catalog (Kauffmann et al. 2003; Brinchmann et al. 2004). Galaxies with BPT classification as AGNs or LINERs are excluded, since certain spectral features (e.g., H α emission) due to nuclear activities might be misinterpreted as star formation.

sion on helium detection in SN 2020jgb. Nonetheless, we discuss other potential strong lines (Mg II, C I, Fe II) that may cause the $1\mu\text{m}$ feature, but have found them also not that likely. Helium is still the most promising candidate for the apparently ubiquitous $1\mu\text{m}$ features.

This paper provides a framework for robust He I detection in He-shell DDet SNe. Ideally, one will need a NIR spectrum covering both the $1\mu\text{m}$ and $2\mu\text{m}$ regions in search of the He I $\lambda 10830$ and $\lambda 20581$ features. Since the He I $\lambda 20581$ is weaker or even invisible when the He-shell is thin (Boyle et al. 2017), and could be blended with strong telluric lines, one should not always expect to see

significant absorption features near $2\mu\text{m}$. For transients showing a clear $1\mu\text{m}$ feature, one can calculate the required velocity assuming an origin in He I $\lambda 10830$ and check if it is comparable with the HVFs velocity in the Ca II IRT absorption at a similar phase. While the detonation recipe in a DDet model and the viewing angles would all affect the observed He I/Ca II velocity, we still expect the elements along the line-of-sight to expand at a similar pace, if they all have a He-shell origin. Excluding the possibility of other strong lines is also necessary. If the NIR spectrum is obtained before the peak of the SN, strong Mg II and C I absorption (Hsiao et al. 2019) would be possible contaminants. Otherwise if the $1\mu\text{m}$ feature is seen in the transitional-phase spectrum when the inner region of the SNe become visible, we need to carefully rule out the possibility of Fe II origin (Marion et al. 2009).

The He-shell DDet SNe in the tiny sample show diversities in various observational properties, including the peak luminosity, color evolution, chemical abundances and line velocities, which could be explained by a large variety of He-shell masses, WD masses, viewing angles, and the initial chemical compositions in the shell. In addition, they are discovered in both old and young stellar populations, SN 2020jgb being the first unambiguous thick He-shell DDet candidate detected in a star-forming galaxy, similar to the normal SNe Ia population. This is in favor of the scenario that a significant fraction of normal SNe Ia are triggered by He-shell DDet. Multiple formation channels and progenitor systems may be required to explain the He-shell DDet population.

Facility: PO:1.2m (ZTF), PO:1.5m (SEDM), Hale (DBSP), NOT (ALFOSC), Shane (Kast Double spectrograph), Keck:I (LRIS), Keck:II (DEIMOS), Gemini:Gillett (GNIRS)

Software: `astropy` (Astropy Collaboration et al. 2013, 2018), `emcee` (Foreman-Mackey et al. 2013), `matplotlib` (Hunter 2007), `prospector` (Johnson et al. 2021), `PyteIt` (Prochaska et al. 2020), `scikit-learn` (Pedregosa et al. 2011), `scipy` (Virtanen et al. 2020), `seaborn` (Waskom 2021).

REFERENCES

- Astropy Collaboration, Robitaille, T. P., Tollerud, E. J., et al. 2013, *A&A*, 558, A33, doi: [10.1051/0004-6361/201322068](https://doi.org/10.1051/0004-6361/201322068)
- Astropy Collaboration, Price-Whelan, A. M., Sipőcz, B. M., et al. 2018, *AJ*, 156, 123, doi: [10.3847/1538-3881/aabc4f](https://doi.org/10.3847/1538-3881/aabc4f)
- Baldwin, J. A., Phillips, M. M., & Terlevich, R. 1981, *PASP*, 93, 5, doi: [10.1086/130766](https://doi.org/10.1086/130766)
- Bellm, E. C., Kulkarni, S. R., Graham, M. J., et al. 2019, *PASP*, 131, 018002, doi: [10.1088/1538-3873/aaecbe](https://doi.org/10.1088/1538-3873/aaecbe)

- Blagorodnova, N., Neill, J. D., Walters, R., et al. 2018, *PASP*, 130, 035003, doi: [10.1088/1538-3873/aaa53f](https://doi.org/10.1088/1538-3873/aaa53f)
- Boyle, A., Sim, S. A., Hachinger, S., & Kerzendorf, W. 2017, *A&A*, 599, A46, doi: [10.1051/0004-6361/201629712](https://doi.org/10.1051/0004-6361/201629712)
- Brinchmann, J., Charlot, S., White, S. D. M., et al. 2004, *MNRAS*, 351, 1151, doi: [10.1111/j.1365-2966.2004.07881.x](https://doi.org/10.1111/j.1365-2966.2004.07881.x)
- Bulla, M., Miller, A. A., Yao, Y., et al. 2020, *ApJ*, 902, 48, doi: [10.3847/1538-4357/abb13c](https://doi.org/10.3847/1538-4357/abb13c)
- Carrick, J., Turnbull, S. J., Lavaux, G., & Hudson, M. J. 2015, *MNRAS*, 450, 317, doi: [10.1093/mnras/stv547](https://doi.org/10.1093/mnras/stv547)
- Cenko, S. B., Fox, D. B., Moon, D.-S., et al. 2006, *PASP*, 118, 1396, doi: [10.1086/508366](https://doi.org/10.1086/508366)
- Chambers, K. C., Magnier, E. A., Metcalfe, N., et al. 2016, *arXiv e-prints*, arXiv:1612.05560. <https://arxiv.org/abs/1612.05560>
- Childress, M. J., Filippenko, A. V., Ganeshalingam, M., & Schmidt, B. P. 2014, *MNRAS*, 437, 338, doi: [10.1093/mnras/stt1892](https://doi.org/10.1093/mnras/stt1892)
- Childress, M. J., Scalzo, R. A., Sim, S. A., et al. 2013, *ApJ*, 770, 29, doi: [10.1088/0004-637X/770/1/29](https://doi.org/10.1088/0004-637X/770/1/29)
- Dahiwal, A., & Fremling, C. 2020, *Transient Name Server Classification Report*, 2020-1624, 1
- De, K., Kasliwal, M. M., Polin, A., et al. 2019, *The Astrophysical Journal*, 873, L18, doi: [10.3847/2041-8213/ab0aec](https://doi.org/10.3847/2041-8213/ab0aec)
- De, K., Kasliwal, M. M., Tzanidakis, A., et al. 2020, *The Astrophysical Journal*, 905, 58, doi: [10.3847/1538-4357/abb45c](https://doi.org/10.3847/1538-4357/abb45c)
- De, K., Kasliwal, M. M., Tzanidakis, A., et al. 2020, *ApJ*, 905, 58, doi: [10.3847/1538-4357/abb45c](https://doi.org/10.3847/1538-4357/abb45c)
- de los Reyes, M. A. C., Kirby, E. N., Seitzzahl, I. R., & Shen, K. J. 2020, *ApJ*, 891, 85, doi: [10.3847/1538-4357/ab736f](https://doi.org/10.3847/1538-4357/ab736f)
- Deckers, M., Maguire, K., Magee, M. R., et al. 2022, *MNRAS*, 512, 1317, doi: [10.1093/mnras/stac558](https://doi.org/10.1093/mnras/stac558)
- Dessart, L., & Hillier, D. J. 2015, *MNRAS*, 447, 1370, doi: [10.1093/mnras/stu2520](https://doi.org/10.1093/mnras/stu2520)
- Dey, A., Schlegel, D. J., Lang, D., et al. 2019, *AJ*, 157, 168, doi: [10.3847/1538-3881/ab089d](https://doi.org/10.3847/1538-3881/ab089d)
- Dong, Y., Valenti, S., Polin, A., et al. 2022, *arXiv e-prints*, arXiv:2206.07065. <https://arxiv.org/abs/2206.07065>
- Duev, D. A., Mahabal, A., Masci, F. J., et al. 2019, *MNRAS*, 489, 3582, doi: [10.1093/mnras/stz2357](https://doi.org/10.1093/mnras/stz2357)
- Eitner, P., Bergemann, M., Ruiter, A. J., et al. 2022, *arXiv e-prints*, arXiv:2206.10258. <https://arxiv.org/abs/2206.10258>
- Elias, J. H., Vukobratovich, D., Andrew, J. R., et al. 1998, in *Society of Photo-Optical Instrumentation Engineers (SPIE) Conference Series*, Vol. 3354, *Infrared Astronomical Instrumentation*, ed. A. M. Fowler, 555–565, doi: [10.1117/12.317281](https://doi.org/10.1117/12.317281)
- Faber, S. M., Phillips, A. C., Kibrick, R. I., et al. 2003, in *Society of Photo-Optical Instrumentation Engineers (SPIE) Conference Series*, Vol. 4841, *Instrument Design and Performance for Optical/Infrared Ground-based Telescopes*, ed. M. Iye & A. F. M. Moorwood, 1657–1669, doi: [10.1117/12.460346](https://doi.org/10.1117/12.460346)
- Filippenko, A. V., Richmond, M. W., Branch, D., et al. 1992, *AJ*, 104, 1543, doi: [10.1086/116339](https://doi.org/10.1086/116339)
- Fink, M., Röpke, F. K., Hillebrandt, W., et al. 2010, *A&A*, 514, A53, doi: [10.1051/0004-6361/200913892](https://doi.org/10.1051/0004-6361/200913892)
- Fitzpatrick, E. L. 1999, *PASP*, 111, 63, doi: [10.1086/316293](https://doi.org/10.1086/316293)
- Foley, R. J. 2015, *MNRAS*, 452, 2463, doi: [10.1093/mnras/stv789](https://doi.org/10.1093/mnras/stv789)
- Foreman-Mackey, D., Hogg, D. W., Lang, D., & Goodman, J. 2013, *PASP*, 125, 306, doi: [10.1086/670067](https://doi.org/10.1086/670067)
- Fremling, C. 2020, *Transient Name Server Discovery Report*, 2020-1247, 1
- Galbany, L., Anderson, J. P., Sánchez, S. F., et al. 2018, *ApJ*, 855, 107, doi: [10.3847/1538-4357/aaaf20](https://doi.org/10.3847/1538-4357/aaaf20)
- Galbany, L., Ashall, C., Hflich, P., et al. 2019, *Astronomy & Astrophysics*, 630, A76, doi: [10.1051/0004-6361/201935537](https://doi.org/10.1051/0004-6361/201935537)
- Geier, S., Marsh, T. R., Wang, B., et al. 2013, *A&A*, 554, A54, doi: [10.1051/0004-6361/201321395](https://doi.org/10.1051/0004-6361/201321395)
- Graham, M. J., Kulkarni, S. R., Bellm, E. C., et al. 2019, *PASP*, 131, 078001, doi: [10.1088/1538-3873/ab006c](https://doi.org/10.1088/1538-3873/ab006c)
- Gronow, S., Collins, C., Ohlmann, S. T., et al. 2020, *A&A*, 635, A169, doi: [10.1051/0004-6361/201936494](https://doi.org/10.1051/0004-6361/201936494)
- Guillochon, J., Parrent, J., Kelley, L. Z., & Margutti, R. 2017, *ApJ*, 835, 64, doi: [10.3847/1538-4357/835/1/64](https://doi.org/10.3847/1538-4357/835/1/64)
- Hsiao, E. Y., Phillips, M. M., Marion, G. H., et al. 2019, *PASP*, 131, 014002, doi: [10.1088/1538-3873/aae961](https://doi.org/10.1088/1538-3873/aae961)
- Hunter, J. D. 2007, *Computing in Science and Engineering*, 9, 90, doi: [10.1109/MCSE.2007.55](https://doi.org/10.1109/MCSE.2007.55)
- Inserra, C., Sim, S. A., Wyrzykowski, L., et al. 2015, *ApJL*, 799, L2, doi: [10.1088/2041-8205/799/1/L2](https://doi.org/10.1088/2041-8205/799/1/L2)
- Jacobson-Galn, W. V., Polin, A., Foley, R. J., et al. 2020, *The Astrophysical Journal*, 896, 165, doi: [10.3847/1538-4357/ab94b8](https://doi.org/10.3847/1538-4357/ab94b8)
- Jha, S. W., Maguire, K., & Sullivan, M. 2019, *Nature Astronomy*, 3, 706, doi: [10.1038/s41550-019-0858-0](https://doi.org/10.1038/s41550-019-0858-0)
- Jiang, J.-a., Doi, M., Maeda, K., et al. 2017, *Nature*, 550, 80, doi: [10.1038/nature23908](https://doi.org/10.1038/nature23908)
- Johnson, B. D., Leja, J., Conroy, C., & Speagle, J. S. 2021, *ApJS*, 254, 22, doi: [10.3847/1538-4365/abef67](https://doi.org/10.3847/1538-4365/abef67)

- Kauffmann, G., Heckman, T. M., White, S. D. M., et al. 2003, *MNRAS*, 341, 33, doi: [10.1046/j.1365-8711.2003.06291.x](https://doi.org/10.1046/j.1365-8711.2003.06291.x)
- Kromer, M., Sim, S. A., Fink, M., et al. 2010, *ApJ*, 719, 1067, doi: [10.1088/0004-637X/719/2/1067](https://doi.org/10.1088/0004-637X/719/2/1067)
- Kupfer, T., Bauer, E. B., van Roestel, J., et al. 2022, *ApJL*, 925, L12, doi: [10.3847/2041-8213/ac48f1](https://doi.org/10.3847/2041-8213/ac48f1)
- Livne, E. 1990, *ApJL*, 354, L53, doi: [10.1086/185721](https://doi.org/10.1086/185721)
- Livne, E., & Arnett, D. 1995, *ApJ*, 452, 62, doi: [10.1086/176279](https://doi.org/10.1086/176279)
- Lunnan, R., Kasliwal, M. M., Cao, Y., et al. 2017, *ApJ*, 836, 60, doi: [10.3847/1538-4357/836/1/60](https://doi.org/10.3847/1538-4357/836/1/60)
- Maguire, K., Sullivan, M., Pan, Y. C., et al. 2014, *MNRAS*, 444, 3258, doi: [10.1093/mnras/stu1607](https://doi.org/10.1093/mnras/stu1607)
- Mahabal, A., Rebbapragada, U., Walters, R., et al. 2019, *PASP*, 131, 038002, doi: [10.1088/1538-3873/aaf3fa](https://doi.org/10.1088/1538-3873/aaf3fa)
- Maoz, D., Mannucci, F., & Nelemans, G. 2014, *ARA&A*, 52, 107, doi: [10.1146/annurev-astro-082812-141031](https://doi.org/10.1146/annurev-astro-082812-141031)
- Marion, G. H., Höflich, P., Gerardy, C. L., et al. 2009, *AJ*, 138, 727, doi: [10.1088/0004-6256/138/3/727](https://doi.org/10.1088/0004-6256/138/3/727)
- Masci, F. J., Laher, R. R., Rusholme, B., et al. 2019, *PASP*, 131, 018003, doi: [10.1088/1538-3873/aae8ac](https://doi.org/10.1088/1538-3873/aae8ac)
- Matheson, T., Filippenko, A. V., Barth, A. J., et al. 2000, *AJ*, 120, 1487, doi: [10.1086/301518](https://doi.org/10.1086/301518)
- Mazzali, P. A., Benetti, S., Altavilla, G., et al. 2005, *ApJL*, 623, L37, doi: [10.1086/429874](https://doi.org/10.1086/429874)
- McMahon, R. G., Banerji, M., Gonzalez, E., et al. 2013, *The Messenger*, 154, 35
- Miller, J., & Stone, R. 1994, *The Kast Double Spectrograph*, Lick Observatory technical reports (University of California Observatories/Lick Observatory). <https://books.google.com/books?id=QXk2AQAAIAAJ>
- Ni, Y. Q., Moon, D.-S., Drout, M. R., et al. 2022, *Nature Astronomy*, doi: [10.1038/s41550-022-01603-4](https://doi.org/10.1038/s41550-022-01603-4)
- Nomoto, K. 1982a, *ApJ*, 253, 798, doi: [10.1086/159682](https://doi.org/10.1086/159682)
- . 1982b, *ApJ*, 257, 780, doi: [10.1086/160031](https://doi.org/10.1086/160031)
- Nugent, P. E., Sullivan, M., Cenko, S. B., et al. 2011, *Nature*, 480, 344, doi: [10.1038/nature10644](https://doi.org/10.1038/nature10644)
- Oke, J. B., & Gunn, J. E. 1982, *PASP*, 94, 586, doi: [10.1086/131027](https://doi.org/10.1086/131027)
- Oke, J. B., Cohen, J. G., Carr, M., et al. 1995, *PASP*, 107, 375, doi: [10.1086/133562](https://doi.org/10.1086/133562)
- Patterson, M. T., Bellm, E. C., Rusholme, B., et al. 2019, *PASP*, 131, 018001, doi: [10.1088/1538-3873/aae904](https://doi.org/10.1088/1538-3873/aae904)
- Pedregosa, F., Varoquaux, G., Gramfort, A., et al. 2011, *Journal of Machine Learning Research*, 12, 2825
- Polin, A., Nugent, P., & Kasen, D. 2019, *ApJ*, 873, 84, doi: [10.3847/1538-4357/aafb6a](https://doi.org/10.3847/1538-4357/aafb6a)
- . 2021, *ApJ*, 906, 65, doi: [10.3847/1538-4357/abccccc](https://doi.org/10.3847/1538-4357/abccccc)
- Poznanski, D., Ganeshalingam, M., Silverman, J. M., & Filippenko, A. V. 2011, *MNRAS*, 415, L81, doi: [10.1111/j.1745-3933.2011.01084.x](https://doi.org/10.1111/j.1745-3933.2011.01084.x)
- Prochaska, J. X., Hennawi, J. F., Westfall, K. B., et al. 2020, *Journal of Open Source Software*, 5, 2308, doi: [10.21105/joss.02308](https://doi.org/10.21105/joss.02308)
- Prochaska, J. X., Hennawi, J., Cooke, R., et al. 2020, *pypeit/PypeIt: Release 1.0.0, v1.0.0*, Zenodo, doi: [10.5281/zenodo.3743493](https://doi.org/10.5281/zenodo.3743493)
- Schlafly, E. F., & Finkbeiner, D. P. 2011, *ApJ*, 737, 103, doi: [10.1088/0004-637X/737/2/103](https://doi.org/10.1088/0004-637X/737/2/103)
- Shahbandeh, M., Hsiao, E. Y., Ashall, C., et al. 2022, *ApJ*, 925, 175, doi: [10.3847/1538-4357/ac4030](https://doi.org/10.3847/1538-4357/ac4030)
- Shen, K. J., Boos, S. J., Townsley, D. M., & Kasen, D. 2021, *ApJ*, 922, 68, doi: [10.3847/1538-4357/ac2304](https://doi.org/10.3847/1538-4357/ac2304)
- Shen, K. J., Kasen, D., Miles, B. J., & Townsley, D. M. 2018, *ApJ*, 854, 52, doi: [10.3847/1538-4357/aaa8de](https://doi.org/10.3847/1538-4357/aaa8de)
- Shen, K. J., & Moore, K. 2014, *ApJ*, 797, 46, doi: [10.1088/0004-637X/797/1/46](https://doi.org/10.1088/0004-637X/797/1/46)
- Shen, K. J., Quataert, E., & Pakmor, R. 2019, *ApJ*, 887, 180, doi: [10.3847/1538-4357/ab5370](https://doi.org/10.3847/1538-4357/ab5370)
- Silverman, J. M., Vinkó, J., Marion, G. H., et al. 2015, *MNRAS*, 451, 1973, doi: [10.1093/mnras/stv1011](https://doi.org/10.1093/mnras/stv1011)
- Silverman, J. M., Foley, R. J., Filippenko, A. V., et al. 2012, *MNRAS*, 425, 1789, doi: [10.1111/j.1365-2966.2012.21270.x](https://doi.org/10.1111/j.1365-2966.2012.21270.x)
- Sim, S. A., Fink, M., Kromer, M., et al. 2012, *MNRAS*, 420, 3003, doi: [10.1111/j.1365-2966.2011.20162.x](https://doi.org/10.1111/j.1365-2966.2011.20162.x)
- Sim, S. A., Röpke, F. K., Hillebrandt, W., et al. 2010, *ApJL*, 714, L52, doi: [10.1088/2041-8205/714/1/L52](https://doi.org/10.1088/2041-8205/714/1/L52)
- Smith, M., Nichol, R. C., Dilday, B., et al. 2012, *ApJ*, 755, 61, doi: [10.1088/0004-637X/755/1/61](https://doi.org/10.1088/0004-637X/755/1/61)
- Sullivan, M., Le Borgne, D., Pritchett, C. J., et al. 2006, *ApJ*, 648, 868, doi: [10.1086/506137](https://doi.org/10.1086/506137)
- Veilleux, S., & Osterbrock, D. E. 1987, *ApJS*, 63, 295, doi: [10.1086/191166](https://doi.org/10.1086/191166)
- Virtanen, P., Gommers, R., Oliphant, T. E., et al. 2020, *Nature Methods*, 17, 261, doi: [10.1038/s41592-019-0686-2](https://doi.org/10.1038/s41592-019-0686-2)
- Waskom, M. L. 2021, *Journal of Open Source Software*, 6, 3021, doi: [10.21105/joss.03021](https://doi.org/10.21105/joss.03021)
- Woosley, S. E., Taam, R. E., & Weaver, T. A. 1986, *ApJ*, 301, 601, doi: [10.1086/163926](https://doi.org/10.1086/163926)
- Woosley, S. E., & Weaver, T. A. 1994, *ApJ*, 423, 371, doi: [10.1086/173813](https://doi.org/10.1086/173813)
- Yaron, O., & Gal-Yam, A. 2012, *PASP*, 124, 668, doi: [10.1086/666656](https://doi.org/10.1086/666656)
- York, D. G., Adelman, J., Anderson, John E., J., et al. 2000, *AJ*, 120, 1579, doi: [10.1086/301513](https://doi.org/10.1086/301513)
- Zackay, B., Ofek, E. O., & Gal-Yam, A. 2016, *ApJ*, 830, 27, doi: [10.3847/0004-637X/830/1/27](https://doi.org/10.3847/0004-637X/830/1/27)